

# 3D Printed MXene Aerogels with Truly 3D Macrostructure and Highly Engineered Microstructure for Enhanced Electrical and Electrochemical Performance

Halil Tetik, Jafar Orangi, Guang Yang, Keren Zhao, Shakir Bin Mujib, Gurpreet Singh, Majid Beidaghi,\* and Dong Lin\*

Assembling 2D materials such as MXenes into functional 3D aerogels using 3D printing technologies gains attention due to simplicity of fabrication, customized geometry and physical properties, and improved performance. Also, the establishment of straightforward electrode fabrication methods with the aim to hinder the restack and/or aggregation of electrode materials, which limits the performance of the electrode, is of great significant. In this study, unidirectional freeze casting and inkjet-based 3D printing are combined to fabricate macroscopic porous aerogels with vertically aligned Ti<sub>3</sub>C<sub>2</sub>T<sub>x</sub> sheets. The fabrication method is developed to easily control the aerogel microstructure and alignment of the MXene sheets. The aerogels show excellent electromechanical performance so that they can withstand almost 50% compression before recovering to the original shape and maintain their electrical conductivities during continuous compression cycles. To enhance the electrochemical performance, an inkjet-printed MXene current collector layer is added with horizontally aligned MXene sheets. This combines the superior electrical conductivity of the current collector layer with the improved ionic diffusion provided by the porous electrode. The cells fabricated with horizontal MXene sheets alignment as current collector with subsequent vertical MXene sheets alignment layers show the best electrochemical performance with thicknessindependent capacitive behavior.

H. Tetik, G. Yang, K. Zhao, D. Lin Department of Industrial and Manufacturing Systems Engineering Kansas State University Manhattan, KS 66506, USA E-mail: dongl@ksu.edu J. Orangi **Product Engineer** Lam Research Fremont, CA 94538, USA S. B. Mujib, G. Singh Department of Mechanical and Nuclear Engineering Kansas State University Manhattan, KS 66506, USA M. Beidaghi Department of Mechanical and Material Engineering Auburn University Auburn, AL 36849, USA

The ORCID identification number(s) for the author(s) of this article

can be found under https://doi.org/10.1002/adma.202104980.

DOI: 10.1002/adma.202104980

E-mail: mzb0088@auburn.edu

## 1. Introduction

The outstanding electronic, mechanical, electrochemical, and optical properties of 2D MXenes, have attracted much research interest since their discovery in 2011.[1] MXenes are transition metal carbides, nitrides, and carbonitrides produced by a selective etching of metal "A" layer atoms from their corresponding "MAX" phases. The term "MAX" phase refers to a group of layered ceramics of the chemical composition of " $M_{n+1}AX_n$ ", where "M" stands for an early transition metal, "A" is an A group element, and "X" is carbon and/or nitrogen.[2-6] MXenes have shown exceptional properties such as high electrical conductivity, hydrophilicity, and the ability to intercalate different cations between their layers. [6-10] However, similar to other 2D materials, the performance of MXenes for some applications is affected by their tendency to restack and/or aggregate during assembly.[11,12] To overcome this issue, various methods are successfully utilized to integrate 2D materials into 3D macroscopic architectures with attractive

properties such as ultralight feature, high porosity, and large specific surface area. [13–15]  $Ti_3C_2T_x$ , which is produced by selective etching of Al atoms from  $Ti_3AlC_2$  MAX phase, is the first discovered and the most studied MXene, [16] and macroscopic 3D porous structures fabricated from  $Ti_3C_2T_x$  and its composites have shown great promise for a variety of applications, [12] including electrochemical energy storage, [15,17–20] electromagnetic interference shielding, [21–27] sensing applications, [28–30] photothermal energy conversion, [31,32] water/oil separation, [33] and solar desalination applications. [34]

Unidirectional freeze casting (UFC) method has been previously utilized for the fabrication of macroscopic 3D porous structures from  ${\rm Ti}_3{\rm C}_2{\rm T}_x$  and its composites. In this method, prepared gels or suspensions of  ${\rm Ti}_3{\rm C}_2{\rm T}_x$  sheets and other components are frozen by applying a unidirectional temperature gradient. Ice crystals nucleate on the cold surface and grow along the temperature gradient.  ${\rm Ti}_3{\rm C}_2{\rm T}_x$  sheets are expelled by the growing ice crystals and aligned along the freezing direction forming a tightly packed continuous network. [24] This well-ordered microstructure obtained after UFC have shown great





www.advmat.de

benefits for a variety of applications. For instance, Bian et al. utilized UFC to fabricate pristine  ${\rm Ti_3C_2T_x}$  aerogels for electromagnetic interference (EMI) shielding applications. [26] Their aerogels' specific shielding effectiveness reached 9904 dB cm³ g⁻¹, which is the highest value reported for foam-like materials. Other studies also reported aerogels that are composites of  ${\rm Ti_3C_2T_x}$  and reduced graphene oxide, [21] sodium alginate, [24] nanocellulose, [25] and gelatin, [27] fabricated through UFC. The high EMI shielding performances of those aerogels are attributed to their ultralight density, high conductivity, and highly ordered porous microstructure. Cai et al. demonstrated that highly ordered microstructures of  ${\rm Ti_3C_2T_x}$ -based aerogels fabricated by UFC are highly efficient for solar absorption and show fast capillarity-driven oil absorption capability. [31]

Moreover, MXene aerogels have been widely explored as electrodes for electrochemical energy storage devices. Engineering electrode structures to enhance their ionic and electronic conductivity can significantly affect the electrochemical properties including rate capability.[12] Yang et al. fabricated porous Ti<sub>3</sub>C<sub>2</sub>T<sub>x</sub> films using UFC to achieve a homogeneous microstructure that is composed of vertically aligned MXene walls within lamellar pores.[35] Supercapacitor electrodes based on the MXene films exhibited remarkably high gravimetric and areal power density of 150 kW kg-1 at 10 00 A g-1 and 667 mW cm<sup>-2</sup> at 4444 mA cm<sup>-2</sup>, respectively. The performance of the Ti<sub>3</sub>C<sub>2</sub>T<sub>x</sub>-based porous supercapacitor electrode films was attributed to the efficient ion transport created by well-ordered microstructure that allows for fast electrochemical charge-discharge cycles. In our previous study, we have demonstrated the critical role of microstructure on the mechanical, electrical, and electrochemical properties of MXene aerogels by fabrication of aerogels with ordered Ti<sub>3</sub>C<sub>2</sub>T<sub>x</sub> sheets through UFC.<sup>[15]</sup> Lithiumion capacitor electrodes made from those aerogels delivered a significantly high specific capacity ( $\approx$ 1210 mAh g<sup>-1</sup> at 0.05 A g<sup>-1</sup>), excellent rate capability (≈200 mAh g<sup>-1</sup> at 10 A g<sup>-1</sup>), and outstanding cycling performance due to their highly ordered and well-engineered microstructure.

Although UFC provided porous Ti<sub>3</sub>C<sub>2</sub>T<sub>x</sub> bodies with wellordered microstructure, which was proven to be beneficial for multiple applications, this method lacks the ability of fabricating porous bodies with complex, engineered macrostructures since it is a mold-based fabrication approach. For applications such as electrochemical energy storage devices, where the geometry, architecture, and micropore morphology of the electrode play a crucial role in the capacitive behavior, fabrication of devices with tailored hierarchical architectures involving micro-, meso-, and macropores is a significant challenge.  $^{[12,1\bar{4},36,37]}$  To address this issue, Li et al. performed the extrusion-based 3D printing and followed with UFC to fabricate thick interdigitated micro-supercapacitors (MSCs) from Ti<sub>3</sub>C<sub>2</sub>T<sub>x</sub>-based aerogels.<sup>[38]</sup> Highly ordered honeycomb-like microporous architectures were obtained after directional freezing facilitated the infiltration of the electrolyte into the internal active sites, which can improve electrochemical performance and also improve resilience to deformation.[38]

Despite the recent advances in 3D printing of MXenes, due to the limitations of extrusion-based 3D printing, truly 3D architectures with overhang features or changing cross-sectional geometry is often difficult to fabricate without using tedious

chemical/thermal post-processes. In the previous reported 3D printed MXene aerogels, extrusion-based 3D printing methods have been used and fabricated structures had to have constant cross-sectional geometries due to lack of support material that can easily be removed after the printing process.<sup>[38–40]</sup> Also, controlling the orientation of MXene sheets in the printed structure has been challenging. As we have demonstrated in this paper, the ability to control the orientation of sheets in both horizontal and vertical directions allows engineering the microstructure of the prints, improve their performance, and extend their applications.

Here, we report on the fabrication of ultralight and truly 3D MXene aerogel structures using 3D freeze-printing (3DFP) method. This novel fabrication method combines UFC and drop-on-demand inkjet printing to tailor the micro- and macrostructure of the aerogels.[41-45] Unlike extrusion-based 3D printing, 3DFP does not require a viscoelastic shear-thinning ink and can use water (ice) as supporting material to fabricate truly 3D structures with overhang features. In this study, we performed mechanical, electrical, and electrochemical characterization of the 3DFP Ti<sub>3</sub>C<sub>2</sub>T<sub>x</sub> aerogels to evaluate their potential for different applications such as piezoresistive sensing, flexible/wearable electronics, and MSC devices. Furthermore, with the advantages provided by our inkjet-based 3D printing method, we fabricated all-MXene MSC devices that are composed of current collector and porous electrodes with controlled orientation of MXene sheets. 3D printed all-MXene MSC devices with engineered microstructure, composed of both horizontally and vertically aligned MXene sheets demonstrated the importance of MXene sheets alignment on the electrochemical performance of the MSCs. The results showed that the current collector layer with horizontally aligned MXenes helps enhancing the electrical conductivity whereas the vertically aligned layer with high porosity provides better ion transport and improved performance at high scan rates. To the best of our knowledge, this is the first report proposing all-solid state MXene MSC devices with both horizontally and vertically aligned MXene sheets. Our results demonstrate 3DFP as a simple, straightforward, and inexpensive electrode fabrication method with great customizability to engineer electrode's micro- and macrostructure.

#### 2. Results and Discussion

 $Ti_3C_2T_x$  aqueous dispersion was prepared following a previously reported method (please see the Experimental Section for a detailed description of the MXene synthesis process and preparation of dispersions). Paielly,  $Ti_3C_2T_x$  was first synthesized by selective etching of Al atoms from  $Ti_3AlC_2$  particles in a LiF and HCl aqueous mixture. The mixture was then washed with DI water until its pH dropped below 5. The product of this washing step was a dilute dispersion of single-layer  $Ti_3C_2T_x$  sheets. Superabsorbing polymer balls were used to adjust the concentration of the dispersion to desired value according to our previously reported method. Figure S1a of the Supporting Information shows an atomic force microscope image of representative single-layer  $Ti_3C_2T_x$  sheets showing an average size of 0.8 μm for MXene sheets. To fabricate  $Ti_3C_2T_x$  aerogels,



ADVANCED MATERIALS

www.advmat.de

droplets of the additive-free aqueous  $Ti_3C_2T_x$  dispersion were generated using an inkjet head (see Figure S2, Supporting Information), and they were deposited onto a freezing substrate at -20 °C (Figure 1a). Droplets are instantly frozen upon contact with the precooled substrate, preserving their shape. By adjusting the interdroplet distance and time lapse between successive droplets, continuous lines were generated through the coalescence of separate droplets. Complex 3D architectures were printed through layer-by-layer deposition of lines (see Video S1, Supporting Information). Once the 3D printing of

the frozen structure is completed, a freeze-drying process was applied to remove the ice from the frozen bodies and achieve highly porous aerogels, as presented in Figure 1b. Figure S1b of the Supporting Information shows a representative X-ray diffraction pattern of a fabricated 3DFP  $\mathrm{Ti_3C_2T_x}$  aerogel, confirming that there is no new phase formation during the 3DFP process.

Since the frozen structures are composed of mostly DI water, after freeze-drying, obtained aerogels are light-weight with a density as low as 9.73 mg cm<sup>-3</sup>. As it is presented in Figure 1c,

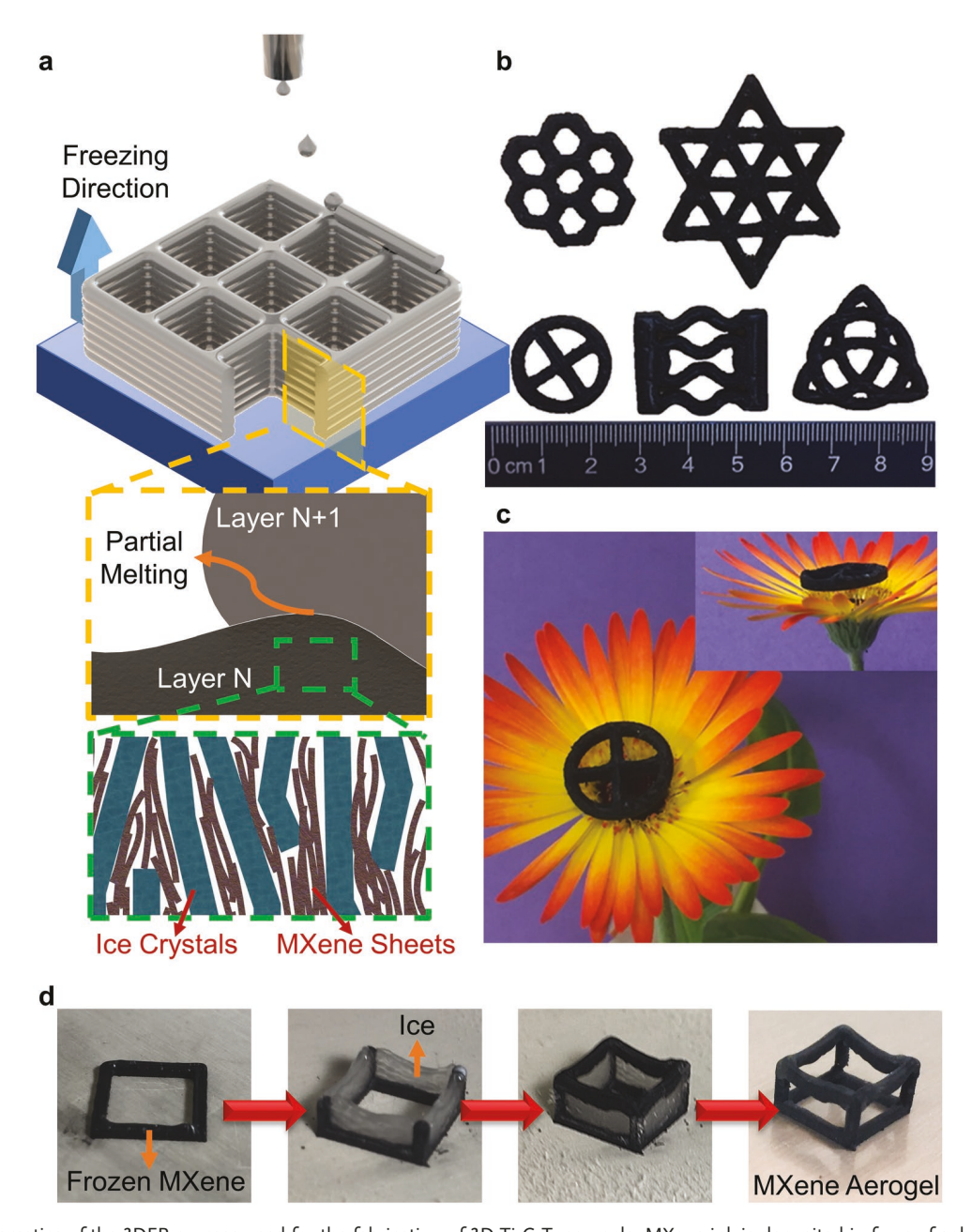


Figure 1. a) Schematics of the 3DFP process used for the fabrication of 3D  $Ti_3C_2T_x$  aerogels. MXene ink is deposited in form of spherical droplets on to a freezing substrate. Partial melting caused by the freshly deposited ink (layer N+1) ensures a good bonding of successive layers. With the freezing of the deposited ink, ice crystals grow from bottom to top, resulting in a vertically aligned porosity and MXene flakes. b) Photograph showing the 3D printed MXene aerogels having various geometries with constant cross-sections. c) Photograph showing 3D printed ultralight aerogels standing on a flower. d) Photographs showing the steps of fabricating truly 3D MXene aerogels with overhang truss structures.





www.advmat.de

3DFP aerogels can stand on a flower without damaging its fibers.

In extrusion-based 3D printing, the physical properties of the prints are negatively influenced by insufficient bonding at the interface of the deposited layers driven by intermolecular diffusion and the undesirable voids between the adjacent layers. [43] In 3DFP, deposited layer at room temperature (N+1<sup>th</sup> layer—Figure 1a) causes a partial melting on top of the previously deposited and frozen layer (Nth layer-Figure 1a). Since the ink's viscosity is low, it fills the possible voids between layers by the help of surface tension and gravitational forces. Finally, partially melted part of Nth layer fuses with the not yet frozen N+1th layer, and they both freeze together. This eliminates insufficient bonding, interfacial boundaries, and voids between layers and yields aerogels with continuous MXene walls as confirmed by the scanning electron microscopy (SEM) images (Figure 2a,b). Furthermore, as in the UFC method, deposited ink on top of the precooled substrate or already frozen layer unidirectionally freezes with ice crystals growing from the bottom to the top along the temperature gradient. This forces the MXene sheets to align vertically forming tightly packed walls between the ice crystals. After freeze-drying, MXene aerogels whose pore morphology is a replica of the ice crystals are obtained.

3D printed Ti<sub>3</sub>C<sub>2</sub>T<sub>x</sub>-based aerogels have previously been fabricated by using extrusion-based 3D printing followed by freeze drying.[38-40] This 3D printing method is limited in printing truly 3D architectures as it is often difficult to print structures with overhang features or changing cross-sectional geometry without using harsh chemical or thermal postprocesses.<sup>[47]</sup> Accordingly, the studies report the fabrication of MXenebased aerogels using extrusion-based 3D printed having a constant cross-sectional geometry, which limits the freedom in design.[38-40] The use of sacrificial support materials that can be burned out after drying process is not practical for MXene due to its oxidation tendency. [48] However, in 3DFP process, ice can be used as the as support material (Figure S3, Supporting Information) to fabricate MXene aerogels with overhang structures (Figure 1d). As we also described in our previous works, [43,45,47] we employed a multinozzle 3D printing setup in which one nozzle was loaded with MXene ink and another nozzle was loaded with DI water as support material. The pillars and trusses of the cube presented in Figure 1d have cross-sectional dimensions of 1 × 1 mm. The length of each truss and the height of each pillar are 10 and 5 mm, respectively. With the 3D printing setup used in this work, the minimum height and thickness of the pillars can be printed are 0.1 and 0.25 mm, respectively. The maximum values of the width and height of the pillars are limited by the build volume of the 3D printing setup (120  $\times$  120  $\times$  120 mm in our setup) provided that the thickness of each pillar is sufficiently large to support the load of the pillars. Also, as we presented in our previous work, [43] the number of the horizontal trusses as well as the number of ice supports between those can be further increased. After sublimation of the ice including the support material during the freeze-drying process truly 3D Ti<sub>3</sub>C<sub>2</sub>T<sub>x</sub> aerogels with overhang features were fabricated. Since 3DFP enables the fabrication of truly 3D MXene aerogels, we believe that this method may lead to new applications for 3D MXene aerogels in the future.

The micropore morphology of the aerogels fabricated through a freeze casting-based method depends on type, concentration, and average size of the solute in the initial suspension, type of the solvent and used additives, and rate of freezing (solidification).<sup>[49]</sup> For instance, Dash et al. showed that the decreasing rate of freezing results in larger average pore size.<sup>[50]</sup>

Yan et al. showed that the solid loading of the initial suspension has a similar impact (e.g., decreasing solid loading resulting in larger average pore size) on the microstructure of the aerogel. [49] Zhang et al. showed how the pore morphology can be tuned by using additives in the initial suspension formulation. [51] With a defined temperature gradient, as in UFC, the nucleation of the ice crystals occurs on the cooled surface and the ice crystals propagate along the temperature gradient. At the end of the freeze-drying process, an aligned pore morphology is obtained. [52] Since 3DFP is a UFC-based fabrication method, the microstructure of the 3DFP aerogels can be tuned using the tools available for UFC, such as solid loading of the ink, temperature of the freezing substrate, using additives in the ink formulation, etc.

The microstructure of aerogels fabricated using 3DFP was studied by SEM, confirming the alignment of the MXene sheets along the temperature gradient from the bottom to the top (Figure 2a-c). With the advantages provided by 3DFP method, void formation is eliminated between subsequent layers and continuous MXene walls all along the freezing direction is obtained (Figure 2a,b). The top surface (plane parallel to the freezing direction) of 3DFP MXene aerogels consists of a micropore morphology with randomly aligned lamellar structures (Figure 2d-f). Depositing the ink in a layer-by-layer fashion did not result in void or boundary formation between deposited layers, indicating the merging of subsequently printed layers into previously printed layers (Figure 2f). The effect of the dispersion concentration on the aerogel's morphology is presented in Figure 2g. With the increasing concentration (from 9 to 15 mg mL<sup>-1</sup>), the porosity decreased, MXene walls became thicker, and the pore width between MXene walls became smaller. This can be related to the less available space for the ice crystals to nucleate and grow and is in good agreement with our previous study reporting the fabrication of MXene aerogels by UFC.<sup>[15]</sup> Changing the microstructure of the aerogels by increasing the concentration of MXene ink would affect mechanical and electrical properties of the fabricated electrodes as discussed below.

 ${\rm Ti_3C_2T_x}$  MXene aerogels and its composites fabricated by conventional methods have been studied as pressure sensors in several previous reports. [13,29,30,53] Using 3D printing to fabricate aerogels can provide flexibility in design and sensor geometry for different applications. To evaluate the performance of the 3DFP MXene aerogels for pressure sensing, we characterized their mechanical and electrical properties (**Figure 3**). For these tests, cubic aerogels ( $5 \times 5 \times 5$  mm) were fabricated using 9, 12, and 15 mg mL<sup>-1</sup> dispersions and their average densities were measured to be 9.73, 12.56, and 15.69 mg cm<sup>-3</sup>, respectively. Mechanical properties of the aerogels were characterized by in-plane compression tests with up to 50% strain (Figure 3a). Three distinctive regimes were observed in the loading curves: a linear elastic region within 0–5% compressive strain, a plateau-like regime between 5% and 30% compressive strain, and

www.advancedsciencenews.com www.advmat.de

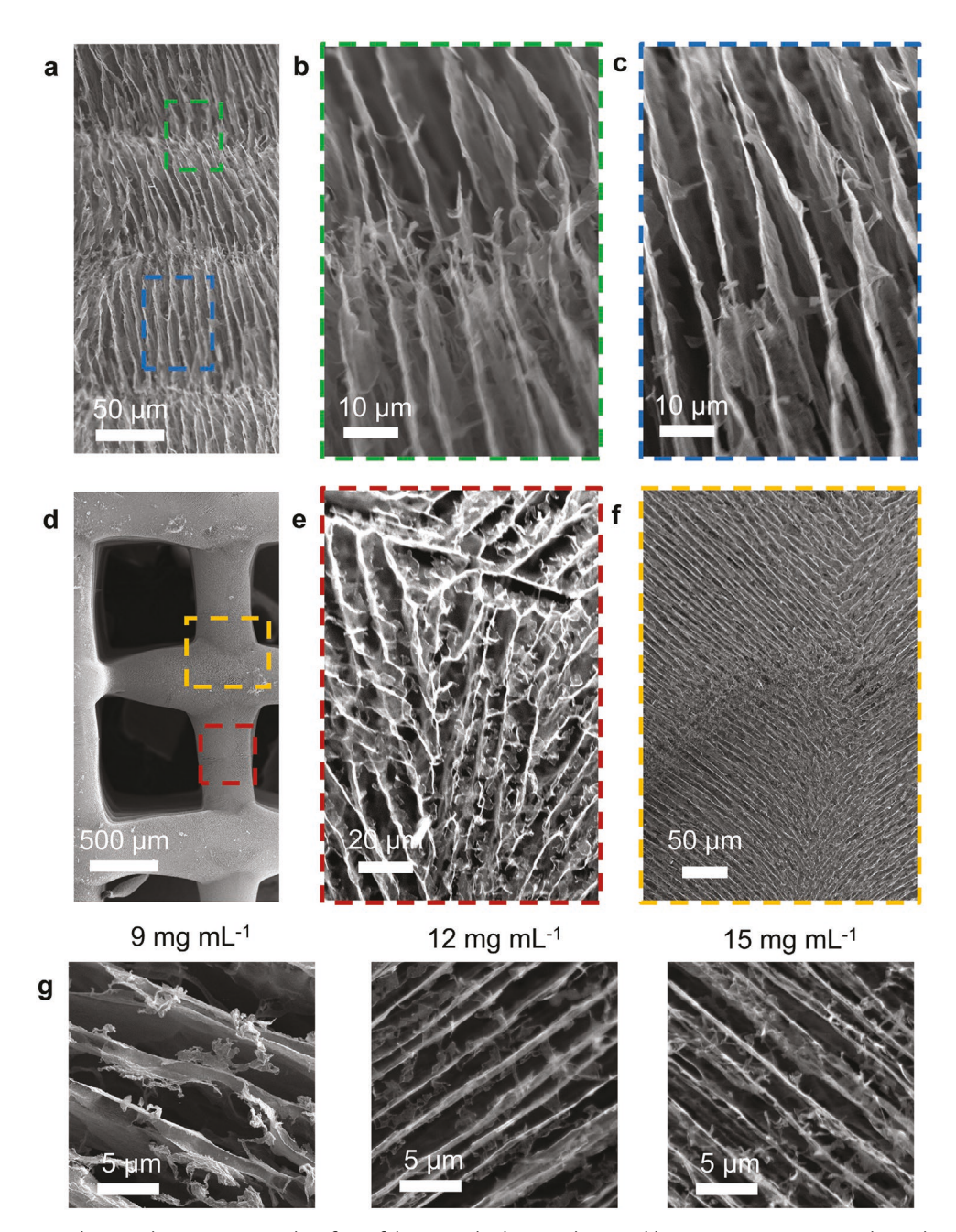


Figure 2. a) SEM image showing the cross-sectional surface of the aerogels showing deposited layers upon previous one. b) High-magnification SEM image showing the layer interface without any voids and interlayer boundaries. c) High-magnification SEM image showing the layer with the aligned porosity along the freezing direction (from bottom to top). d) SEM image showing the top surface of the 3D freeze printed MXene aerogels. e) High-magnification SEM image showing the random pore alignment on the plane perpendicular to freezing direction. f) High-magnification SEM image showing no visible boundary between grids deposited one after another. g) Images showing the top surface of 3DFP MXene aerogels fabricated from inks with a concentration of 9, 12, and 15 mg mL<sup>-1</sup>.

a nonlinear elastic regime after 30% compressive strain. The maximum stresses at 50% strain were measured as 1.3, 2.25, and 4.04 kPa with the increasing density values. This trend was in good agreement with previously reported 3DFP aerogels  $^{[42,43]}$  and freeze casted pristine  $\mathrm{Ti}_3\mathrm{C}_2\mathrm{T}_x$  aerogels.  $^{[15,22]}$ 

The mechanical response of the 15.69 mg cm<sup>-3</sup> aerogel, which provided the highest stress response at 50% compressive strain value, was further studied using five-stepped compressive

loading–unloading strains up to 50% strain with 10% increments (Figure 3b). The results indicate that the succeeding stress–strain curves almost rise back to the stress level measured at the maximum strain value of the previous cycle. This trend was repeated for all increment values indicating an excellent strain memory effect.<sup>[54]</sup> Multicycle compression test further revealed the great resilience of the 3DFP MXene aerogels. 3D freeze printed specimens were compressed for 50 cycles up

www.advmat.de

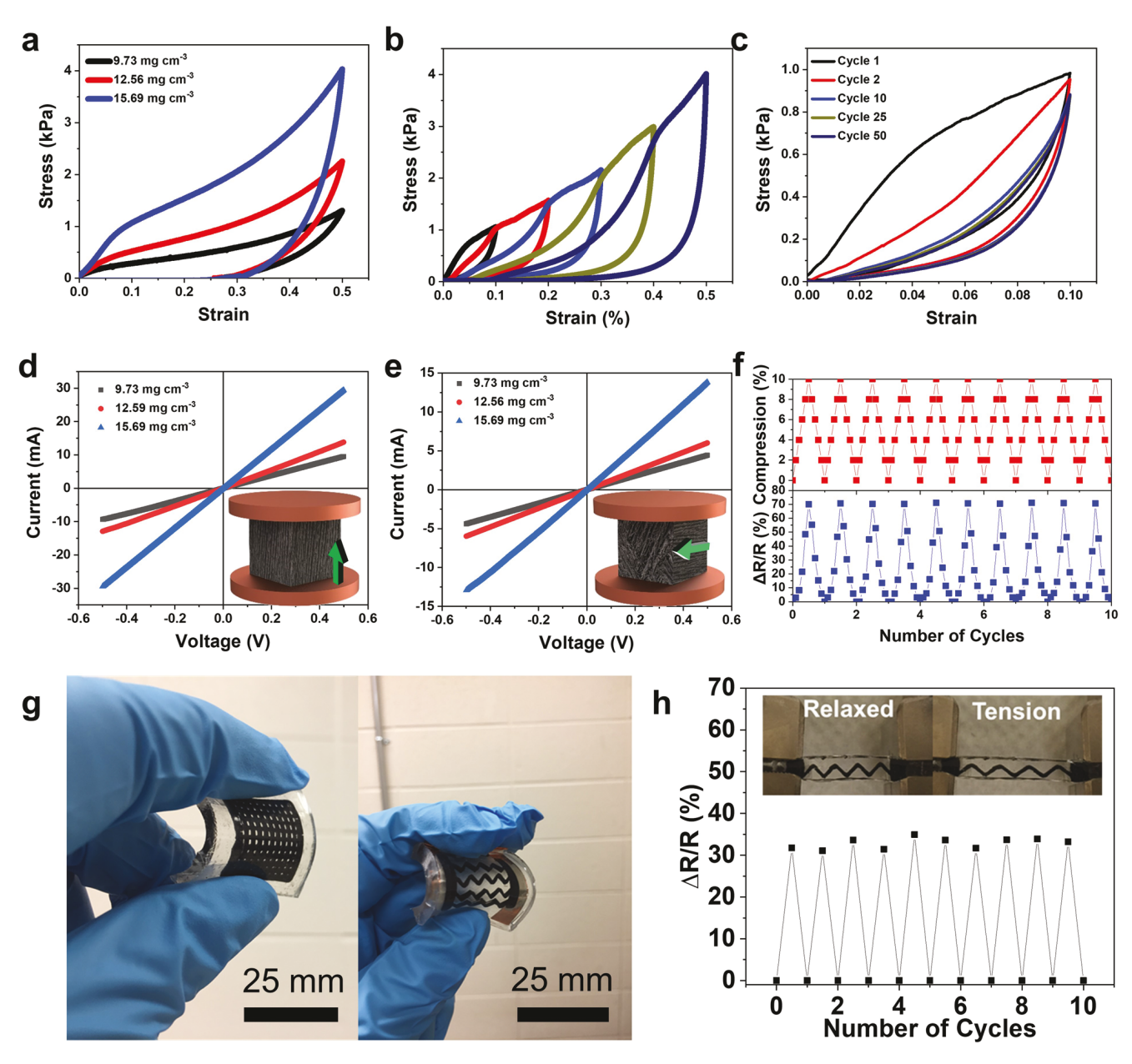


Figure 3. Mechanical and electrical properties of 3DFP MXene aerogels. a) Stress–strain plots of the aerogels having different densities after uniaxial compression tests up to 50% compressive strain. b) Stress–strain curves of multicycle compression by increasing strain amplitude of printed MXene aerogels ( $\rho = 15.69 \text{ mg cm}^{-3}$ ). c) Stress–strain curves for 50 loading–unloading cycles up to 10% strain ( $\rho = 15.69 \text{ mg cm}^{-3}$ ). d) I-V curves of  $Ti_3C_2T_x$  aerogels with different densities parallel to freezing direction. e) I-V curves of  $Ti_3C_2T_x$  aerogels with different densities perpendicular to freezing direction. The arrows in the inset of both (d) and (e) indicate the freezing direction. f) Response in the aerogels resistance to a compression with 10% strain for 10 consecutive cycles ( $\rho = 15.69 \text{ mg cm}^{-3}$ ). g) 3D freeze printed MXene aerogels infiltrated in PDMS elastomer. h) Response in the resistance of the 3D freeze printed aerogels infiltrated in PDMS after applying 10% tension.

to 10% strain to further investigate the mechanical robustness of the structure (Figure 3c). The second loading–unloading curve exhibited a stress degradation less than 3%, meaning that the 3DFP MXene aerogels maintain their original elasticity and structural robustness. After 15 loops, the stress response at 10% strain was stabilized at  $\approx$ 0.87 kPa (Figure S4, Supporting Information), which corresponds to an 11.2% stress decay.

The electrical conductivity of the fabricated cubic specimens as a function of their density was investigated using current (*I*)-voltage (*V*) curves. In Figure 3d,e, the MXene aerogels were placed between two copper electrodes so that the freezing direction is parallel and perpendicular to the testing direction, respectively. The current responses of all specimens in all directions present a linear relationship with the changing voltage, following Ohm's law. Since the microstructural features of the aerogels, such as the thickness of MXene walls or the distance between the walls, have a great dependency on the density of aerogels, the resistance of the specimens increased with





www.advmat.de

decreasing density due to the presence of more space and less intersheet junctions in the microstructure. A similar behavior was also observed in our previous study reporting  $Ti_3C_2T_x$  aerogels fabricated through the UFC method. The Joppen MXene aerogels in parallel configuration (measurement in the direction of freezing) exhibited high electrical conductivity values: 3.78, 5.35, and 11.8 S m<sup>-1</sup> at densities of 9.73, 12.56, and 15.69 mg cm<sup>-3</sup>, respectively (Figure 3d). When the freezing direction of the aerogels are perpendicular to the copper plates (measurement in the direction perpendicular to freezing), the conductivity of the samples reduced to 1.76, 2.40, and 5.35 S m<sup>-1</sup> for 9.73, 12.56, and 15.69 mg cm<sup>-3</sup> samples, respectively. This anisotropy in the electrical conductivity of the 3D freeze printed aerogels due to unidirectional freezing is in good agreement with the previous reports.

To further characterize the piezoresistive behavior of the 3DFP aerogels, in situ resistance measurement was employed over 10 cycles of mechanical compression up to 10% strain value. Electrical resistance of the fabricated aerogels is highly stable over multiple cycles, indicating a significant structural resilience (Figure 3f).<sup>[55]</sup> Inspired by the work of Wang et al.,<sup>[56]</sup> 3DFP MXene aerogels were infiltrated in poly(dimethylsiloxane) (PDMS) elastomer to provide improved performance for real world applications such as wearable electronics. As seen in Figure 3g, we printed MXene aerogels where the user can control the shape and dimensions of the inner features. After infiltration of the PDMS into the pores of the MXene aerogels and curing, we have obtained flexible composites with a conductive MXene network, whose shape and dimensions can be customized for various needs. MXene/PDMS composites showed a great elasticity and a stable response in the electrical resistance (≈30% change in the resistance) with the applied tension (10% strain) for 10 consecutive cycles (Figure 3h).

In order to demonstrate the potential of 3DFP MXene aerogels for energy storage application, interdigitated Ti<sub>3</sub>C<sub>2</sub>T<sub>x</sub> electrodes were printed (using 15 mg mL<sup>-1</sup> dispersion) on various substrates (including paper, acetate film, acrylic sheet, and glass slide), and their performance as all-solid state MSCs were investigated (Figure S5, Supporting Information). The dimensions of the printed MSCs are provided in Figure S6 of the Supporting Information. Due to the nature of the 3DFP process, fabricated interdigitated electrodes possessed a highly ordered porous morphology with vertically aligned MXene sheets (Figure S7, Supporting Information). The ordered and vertically aligned microstructure of the printed electrodes leads to their enhanced electrical and ionic conductivities, improving the capacitance and rate handling capability of the printed devices.[35,57] However, due to the anisotropic microstructure of the MXene aerogels, the electrical conductivity is also anisotropic as discussed above (Figure 3d,e). Considering the geometry of the fabricated MSCs, in-plane electrical conductivity (x–y plane) is expected to be much lower than out-of-plane (y-z or x-z planes) due to the vertical alignment of the MXene sheets (see Figure S8, Supporting Information). Cuna et al. have previously showed that the electrical conductivity as well as specific capacitance of electrodes having an anisotropic porosity is highly dependent on the testing direction.<sup>[58]</sup>

To address this issue and increase the electrical conductivity in x–y plane, we added a current collector layer to the electrode

design. To achieve that, the same 3D printing setup was employed while the substrate was kept at ambient temperature. We first performed inkjet-based printing of a current collector layer and let it dry in ambient conditions to obtain MXene film with horizontally aligned sheets. Following, the temperature of the substrate was reduced to the desired value and 3DFP was performed to achieve porous electrodes standing on the current collector layer (Figure S9, Supporting Information). The resulting MSCs had a hybrid alignment of MXene sheets: the current collector with horizontally aligned sheets followed by the porous electrode with vertically aligned MXene sheets (Figure S10, Supporting Information). The current collector layer with horizontally aligned MXene sheets provided superior electrical conductivity along x-y plane (Figure S8, Supporting Information) whereas the porous electrode with vertically aligned MXene sheets provided an improved ionic diffusion and electrical conductivity in z direction. As previously reported by Peng et al.,[59] all-MXene MSCs exhibit a much lower contact resistance, higher capacitances, and better ratecapabilities compared to MXene MSCs with platinum current collectors.

To evaluate the performance of fabricated MXene-based MSCs and study the effect of MXene sheets alignment on the electrochemical performance, 3D devices with horizontal, vertical, and mixed alignment of the MXene sheet were fabricated. The fabricated devices were labeled based on the number of printed layers as MSC-XH-YV, where X and Y represent the number of printed layers with horizontal (H, air dried) and vertical (V, freeze printed/dried) sheet alignment, respectively (e.g., MSC-1H-3V consists of one layer of air dried and three layers of freeze printed structure). The CV curves of the MSC-2H-1V device at different scan rates show an ideal capacitive behavior with a quasi-rectangular shape as presented in Figure 4a. To test the flexibility of the MSC devices, the effect of bending on their electrochemical performance of the MSC-3V devices printed on paper substrate was investigated (Figure S11, Supporting Information). CV curves at 50 mV s<sup>-1</sup> and electrochemical impedance spectroscopy (EIS) tests results at different bending angles (60°, 120°, and 180°) are presented in Figure S11 of the Supporting Information. The flexibility of the printed devices is demonstrated by the capacitance, and series resistance (Rs) of the MSC not changing significantly with changing the bending angle. MSCs with different current collector-electrode layer combinations showed similar CV curve shapes at different scan rate (Figure 4b; Figure S12, Supporting Information, CV at 10 mV s<sup>-1</sup>). The specific capacitance of the devices with different number of printed layers at different scan rates is presented in Figure 4c. As expected, increasing the load of active material per area results in a higher areal capacitance. The MCS-1H, MCS-1H-1V, MCS-1H-3V, MCS-1H-5V, and MCS-2H-1V devices showed high areal capacitance of 13, 35, 48.2, 79, and 63 mF cm<sup>-2</sup>, respectively (Figure 4c). The results indicate that designing electrode structure through changing the MXene sheets orientation significantly affect electrochemical performances.[12]

Comparing the electrochemical properties of MSC-1V (superior capacitive performance at higher scan rates) and MSC-1H (superior capacitive performance at lower scan rates) helps to better understand the influence of sheet alignment (Figure 4d).

www.advmat.de

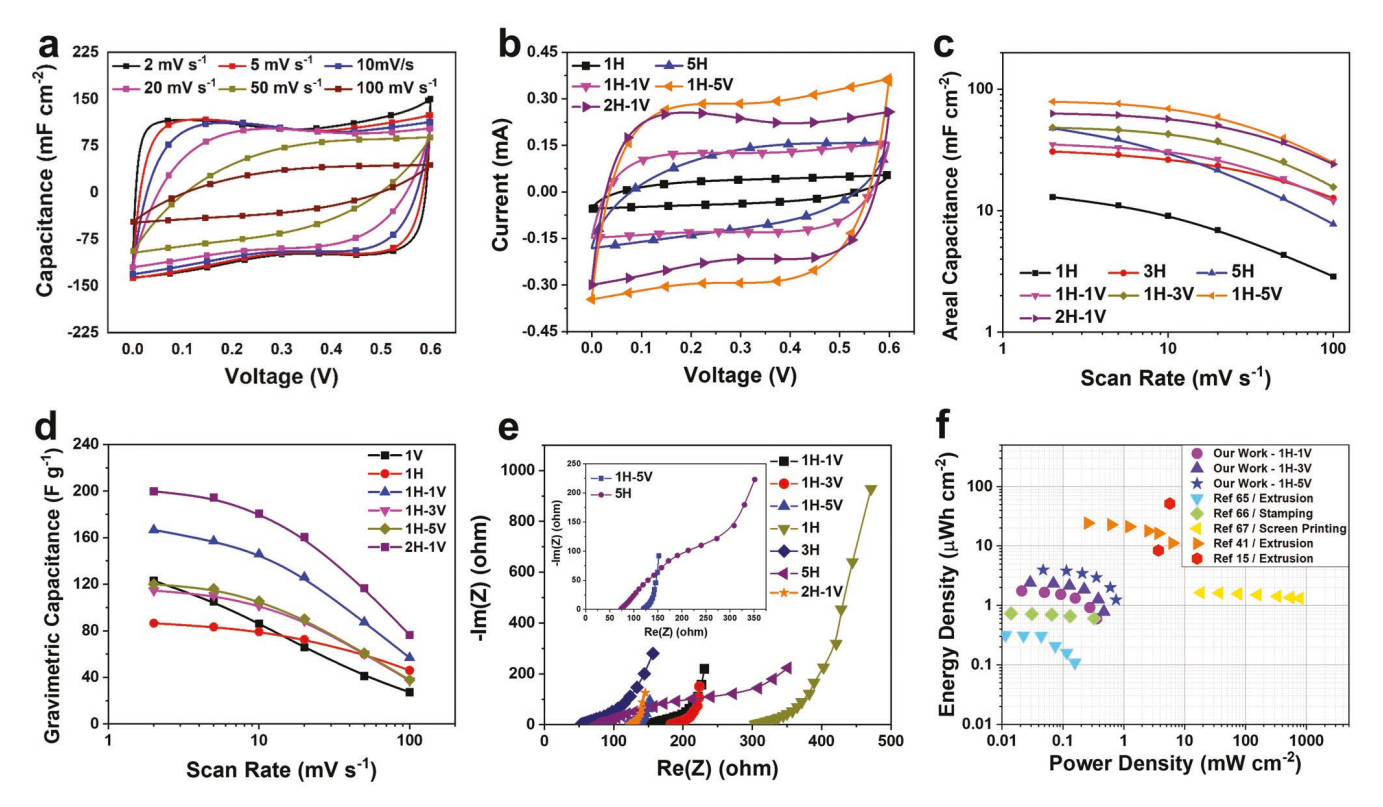


**Figure 4.** Electrochemical performance of 3DFP MXene-based MSC. a) CV at different scan rate for MSC-2H-1V. b,c) CV curves at 10 mV s<sup>-1</sup> and areal capacitance of different 3DFP MSC devices. d) Gravimetric capacitance of MXene-based MSC compared with different MXene-based film with different thicknesses and sheets alignment. e) Nyquist plots for different MXene MSCs taken at 0 V versus the open-circuit potential. The inset shows the Nyquist plots of the MSC-5H and MSC-1H-5V. f) Ragone plots of the 3DFP  $Ti_3C_2T_x$ -based MSCs together with other reported values for comparison.

At low scan rates ionic transfer is the dominant factor on the electrochemical performance, while at high scan rates the role of electron transfer is dominant. The results show that MSC-1H has better electron transfer properties (in agreement with aforementioned electrical conductivity results), while for the MSC-1V ionic transfer is enhanced. MSC-2H-1V showed high gravimetric capacitance of ≈200 F g<sup>-1</sup> at 2 mV s<sup>-1</sup> due to its improved ionic and electronic transfer properties. In addition, increasing the electrode thickness from 626 to ≈925 µm for MSC-1H-3V and MSC-1H-5V did not affect the gravimetric capacitive behavior of the devices, indicating the thickness independent-behavior. The freeze printed MSCs surpasses some of the best gravimetric capacitive performances reported in literature (Table S1, Supporting Information). [57,60-70] This behavior can be related to the increased amount of accessible MXene surface area in the vertically aligned structure and enhanced electrical conductivity due to the horizontally aligned sheets in the current collector layer.

As previously discussed by Yang et al., vertical alignment of the MXene sheets may reduce their restacking while preserving a high porosity in the structure resulting in a highly ion accessible the electrodes.<sup>[35]</sup> Directional ion transport, parallel to the direction of sheets, also leads to a thickness independent behavior of the electrodes.<sup>[57]</sup> On the other hand, the horizontally aligned current collector layer provides enhanced electrical conductivity due to its closely packed MXene sheets that are oriented in direction of electron flow from the device electrical

connection to the interdigital electrodes.<sup>[71]</sup> The advantage of the dual alignment of the sheet on the charge storage properties of MSCs is schematically presented in Figure S13 of the Supporting Information. Once ion reaches the surface MXene sheets, the charge is stored by the reversible protonation of surface functional groups. In a simplified view, the overall charge—discharge process can be expressed as Equation (1)<sup>[72]</sup>

$$\operatorname{Ti}_{3}C_{2}O_{x}(OH)_{y}F_{z} + H^{+} + SO_{4}^{2-} = \left[\operatorname{Ti}_{3}C_{2}O_{x}(OH)_{y}F_{z}\right]^{-} / / H^{+} + \left[\operatorname{Ti}_{3}C_{2}O_{x}(OH)_{y}F_{z}\right]^{+} / / SO_{4}^{2-}$$
(1)

where  $H^+$  and  $SO_4^{2-}$  are the cation and the anion present in the PVA/ $H_2SO_4$  electrolyte.

The fabricated devices showed excellent cyclability, retaining  $\approx$ 94% of their capacitance after 10 000 cycles (Figure S14, Supporting Information). It is worth highlighting the importance of the horizontally aligned layers (the current collector) in device integrity and physical stability. The vertically aligned MXene sheets did not have a good attachment to the substrate.

To compare the maximum areal capacitance value of the 3DFP MSC-1H-5V (79 mF cm<sup>-2</sup>), we prepared the plot given in Figure S15 of the Supporting Information. This compares the maximum areal capacitance values reported for interdigitated electrode structures fabricated from solely MXene inks. It shows that 3DFP results in a higher areal capacitance by



ADVANCED MATERIALS

www.advmat.de

keeping the initial ink concentration the same when compared to other fabrication methods.

EIS test was employed to further study the charge transfer and ion transport in the 3DFP MSCs with their porous and well aligned architecture. As presented in Figure 4e and Figure S16 (Supporting Information) Rs was decreased from  $\approx\!550~\Omega~cm^{-2}$  for MSC-1V to  $\approx\!300~\Omega~cm^{-2}$  for MSC-1H to ≈150  $\Omega$  cm<sup>-2</sup> for MSC-1H-1V, and to ≈120  $\Omega$  cm<sup>-2</sup> for MSC-2H-1V with MXene sheets working as current collector, indicating the importance of horizontally aligned layers. The EIS results of MSC-5H and MSC-1H-5V are presented in inset of Figure 4e. While the MSC-5H showed lower Rs, the MSC-1H-5V showed improved ionic transfer confirmed by higher slope of the Nyquist plot in the low frequency regime. [57,60] This originated from the vertical versus horizontal alignment of the MXene sheets. The vertically aligned MXene sheets possess faster ion transport compared with horizontally aligned electrodes due to their well aligned porous structure, which is a key element for thickness-independent performance. It is worth mentioning the lack of noticeable semicircle in high frequency region, indicating low charge transfer resistance for all the tested samples. These results are in line with the morphological studies of the electrodes confirming the formation of a well aligned porous structure for MSC fabricated with 3DPF process.

The Ragone plot (Figure 4f) further showcases the potential of 3DFP MXene interdigitated electrodes for high energy density and power density supercapacitors.  $^{[14,39,73-75]}$  At a scan rate of 50 mV s $^{-1}$ , the MSC-1H-5V exhibits an energy density of 2  $\mu$ Wh cm $^{-2}$  and a power density of 0.6 mW cm $^{-2}$ . By decreasing scan rate to 2 mV s $^{-1}$ , the energy density increases to 3.9  $\mu$ Wh cm $^{-2}$  while the power density decreases to 0.05 mW cm $^{-2}$ . The 3DFP,  $Ti_3C_2T_x$ -based MSCs exhibit almost ten orders of magnitude higher energy density with comparable power densities to other reported MSC devices with similar power density values. The electrochemical performances indicate that designing electrode structure through changing the MXene sheets orientation significantly affects electrochemical performances.  $^{[12]}$ 

#### 3. Conclusions

This study reports on fabrication of ultralight, multipurpose, and truly 3D MXene aerogel structures using 3DFP method. While simple, straightforward, and inexpensive, the proposed fabrication method provides a great deal of customizability to engineer the micro- and macrostructure of the fabricated electrodes. Employing this capability and study electrodes properties with different microstructure provided a better insight into structure-property relationship. The mechanical compression tests showed that the aerogels' mechanical properties can be tuned simply by controlling the ink concentration. The excellent stability of the electrical conductivity over multiple compression cycles revealed excellent structural resilience of the fabricated aerogels. The all-MXene based 3DFP MSCs with various sheets alignment showed improved capacitive and rate capability responses and confirmed the importance of engineering microstructure and its effect on electrochemical performances. The engineered MSCs with hybrid MXene sheets

orientation showed thickness independent capacitive behavior. The proposed fabrication method can be employed to fabricate various devices with enhanced performances in applications such as flexible electronics, sensors, and energy storage.

# 4. Experimental Section

Preparation of  $Ti_3C_2T_x$  Dispersions:  $Ti_3C_2T_x$  dispersions were prepared according to a previously reported method. [46] Briefly, concentrated hydrochloric acid (HCl, ACS Grade, BDH) solution was diluted with DI water to obtain 20 mL of 9 m HCl solution. About 1.6 g lithium fluoride (LiF, 98+% purity, Alfa Aesar) was added to the solution and stirred for 10 min using Teflon-coated magnetic stir bars at room temperature. Then, 1 g of  $Ti_3AlC_2$  powder was slowly added to the solution. The mixture was transferred to a hot bath and kept at 35 °C for 24 h while stirring. The mixture was then washed several times with DI water and centrifuged at 3500 rpm until the supernatant pH reaches ≈6. The supernatant in each washing step was collected and the concentration was adjusted to desired values using superabsorbing polymer balls. [14] The dispersion then used to print all MXene-based aerogels and MSC electrodes. [14]

Freeze Printing: Details of the 3D printing setup<sup>[76]</sup> and 3DFP process<sup>[47]</sup> were explained in the previous reports. Briefly, a 3-axis motion stage (Panowin Technologies, Shanghai, China) was used to manipulate the inkjet printing head, which was composed of a syringe barrel (Nordson EFD, RI, USA) and a solenoid inkjet dispenser (The Lee Co, CT, USA) connected to a 100 μm nozzle tip. Ti<sub>3</sub>C<sub>2</sub>T<sub>x</sub> suspension with various concentrations was loaded inside the syringe barrel and the internal pressure was controlled using a pneumatic fluid dispenser (Nordson EFD, RI, USA). Droplets of Ti<sub>3</sub>C<sub>2</sub>T<sub>x</sub> suspension that were generated by the inkjet dispenser were deposited on to the substrate whose temperature was controlled by liquid nitrogen (LN2) operated hot/cold plate (Instec, CO, USA). Silicon wafer substrates (unless otherwise specified) and a cold plate temperature of -20 °C were used. Once 3D freeze printing of samples was completed, they were freeze dried by a commercially available freeze dryer (Labconco, MO, USA) at -35 °C and 0.02 mbar for at least 48 h.

Material Characterization: The microstructure of the 3DFP Ti<sub>3</sub>C<sub>2</sub>T<sub>x</sub> aerogels was investigated by SEM (FEI HELIOS Nanolab 600i, OR, USA). For mechanical, electrical, and thermoelectrical characterization, cubic samples with dimensions of  $5 \times 5 \times 5$  mm were fabricated using MXene dispersions with concentrations of 9, 12, and 15 mg mL<sup>-1</sup>. For in-plane compression tests, a digital material testing device (Shimadzu Universal Testing Machine, Kyoto, Japan) was used. All the compression tests were performed with a constant compression rate of 1 mm min<sup>-1</sup> The V-I plots for obtaining the electrical conductivity properties of the MXene aerogels were obtained using a CHI 760D electrochemical workstation (CH Instruments, Austin, TX). For determination of the piezoelectric behavior, the resistance of the aerogels was measured by a two-probe method using a digital multimeter (Fluke 287) by a sampling interval of 2 Hz. The electrodes were painted with high conductive silver paste ( $\approx$ 0.01  $\Omega$  cm) on two sides of the samples to eliminate contact resistance. All the samples were placed between the compression (for mechanical characterization) or copper plates (for electrical characterization) so that the freezing direction is parallel to the surface normal of compression/copper plates unless otherwise stated.

Symmetrical MSCs were 3DFP using 15 mg mL $^{-1}$  dispersion and their electrochemical performances were tested using a VMP3 potentiostat (Biologic, France). Pieces of silver wire were used to connect the printed electrodes to the potentiostat cables. Silver adhesive (fast-drying Ag paint, SPI Supplies) was used to connect silver wires with the current collectors/electrodes. To cover the contact area to protect the silver paint and wires from the electrolyte, nail polish was used. The PVA/  $H_2SO_4$  gel electrolyte was carefully drop cast onto the printed  $Ti_3C_2T_x$  interdigital electrodes design followed by air drying overnight. To avoid MXene oxidation, cyclic voltammetry tests were performed at scan rates ranging from 2 to 100 mV s $^{-1}$  in a potential window of 0 to 0.6 V.[ $^{17}$ ]





www.advmat.de

Electrochemical impedance spectroscopy was performed at open-circuit potential, with a small sinusoidal amplitude of 5 mV, and frequencies of 10 mHz to 100 kHz. The areal and gravimetric capacitances were calculated for the printed devices.<sup>[77]</sup>

The CV curve was used to calculate the cell capacitance (C/A), according to the following equations

$$C = \frac{\int I(V) dV}{v \cdot \Delta V} [F], \text{ (two-electrode configuration)}$$
 (2)

where I(V) was the voltammetric discharge current (mA), v is the scan rate (mV s<sup>-1</sup>), and  $\Delta V$  is the potential window (0.6 V).

The normalized areal (C/A) and gravimetric (C/G) capacitances were calculated based on the area  $(A, \text{ in cm}^2 \text{ calculated as the total area of the device)}$  and total weight of the printed devices. The normalized capacitances were calculated as follows

$$C/A = \frac{C_{\text{device}}}{A} \tag{3}$$

anc

$$C/G = \frac{C_{\text{device}}}{g} \tag{4}$$

The power and energy densities of the devices were measured according to the following equations

Energy density(E) = 
$$\frac{((C/A) \times V^2)}{7200} [Wh cm^{-2}]$$
 (5)

Power density(P) = 
$$\frac{3.6 \times E \times v}{V}$$
 [W cm<sup>-2</sup>] (6)

where C/A [F cm<sup>-2</sup>], V [V], and v [mV s<sup>-1</sup>] are as described above.

## Supporting Information

Supporting Information is available from the Wiley Online Library or from the author.

#### **Acknowledgements**

H.T. and J.O. contributed equally to this work. H.T. acknowledges the graduate research scholarship from the Turkish Ministry of National Education. J.O. acknowledges the support from the Alabama EPSCoR Graduate Research Scholar Program (GRSP Round 12, 13, and 14) doctoral fellowship. M.B. acknowledges the support by a National Science Foundation grant (OAI-1929195). D.L. thanks to the support from the National Science Foundation under Award No. 1943445, NASA EPSCoR Cooperative Agreement Notice (Award No. 80NSSC19M0153), the Kansas NASA EPSCoR Research Infrastructure Development Program (Award No. 80NSSC19M0042), and the support from Johnson Cancer Center.

#### **Conflict of Interest**

The authors declare no conflict of interest.

## **Data Availability Statement**

The data that support the findings of this study are available on request from the corresponding author. The data are not publicly available due to privacy or ethical restrictions.

# **Keywords**

3D freeze printing, all-MXene micro-supercapacitors, MXene aerogels, ordered microstructures, piezoresistive sensing and flexible electronics

Received: June 29, 2021 Revised: August 9, 2021 Published online:

- [1] M. Naguib, M. Kurtoglu, V. Presser, J. Lu, J. Niu, M. Heon, L. Hultman, Y. Gogotsi, M. W. Barsoum, Adv. Mater. 2011, 23, 4248.
- [2] M. Naguib, V. N. Mochalin, M. W. Barsoum, Y. Gogotsi, Adv. Mater. 2014, 26, 992.
- [3] M. Naguib, O. Mashtalir, J. Carle, V. Presser, J. Lu, L. Hultman, Y. Gogotsi, M. W. Barsoum, ACS Nano 2012, 6, 1322.
- [4] B. Anasori, M. R. Lukatskaya, Y. Gogotsi, Nat. Rev. Mater. 2017, 2, 16098.
- [5] M. Naguib, J. Come, B. Dyatkin, V. Presser, P.-L. Taberna, P. Simon, M. W. Barsoum, Y. Gogotsi, Electrochem. Commun. 2012, 16, 61.
- [6] B. Anasori, Y. Xie, M. Beidaghi, J. Lu, B. C. Hosler, L. Hultman, P. R. Kent, Y. Gogotsi, M. W. Barsoum, ACS Nano 2015, 9, 9507.
- [7] J. Halim, S. Kota, M. R. Lukatskaya, M. Naguib, M. Q. Zhao, E. J. Moon, J. Pitock, J. Nanda, S. J. May, Y. Gogotsi, Adv. Funct. Mater. 2016, 26, 3118.
- [8] X. Wang, S. Kajiyama, H. Iinuma, E. Hosono, S. Oro, I. Moriguchi, M. Okubo, A. Yamada, Nat. Commun. 2015, 6, 6544.
- [9] J.-C. Lei, X. Zhang, Z. Zhou, Front. Phys. 2015, 10, 276.
- [10] D. Er, J. Li, M. Naguib, Y. Gogotsi, V. B. Shenoy, ACS Appl. Mater. Interfaces 2014, 6, 11173.
- [11] T. Shang, Z. Lin, C. Qi, X. Liu, P. Li, Y. Tao, Z. Wu, D. Li, P. Simon, Q. H. Yang, Adv. Funct. Mater. 2019, 29, 1903960.
- [12] J. Orangi, M. Beidaghi, Adv. Funct. Mater. 2020, 30, 2005305.
- [13] J. Liu, H. B. Zhang, X. Xie, R. Yang, Z. Liu, Y. Liu, Z. Z. Yu, Small 2018, 14, 1802479.
- [14] J. Orangi, F. Hamade, V. A. Davis, M. Beidaghi, ACS Nano 2019, 14, 640.
- [15] J. Orangi, H. Tetik, P. Parandoush, E. Kayali, D. Lin, M. Beidaghi, Mater. Today Adv. 2021, 9, 100135.
- [16] K. Hantanasirisakul, M. Alhabeb, A. Lipatov, K. Maleski, B. Anasori, P. Salles, C. Ieosakulrat, P. Pakawatpanurut, A. Sinitskii, S. J. May, Chem. Mater. 2019, 31, 2941.
- [17] J. Song, X. Guo, J. Zhang, Y. Chen, C. Zhang, L. Luo, F. Wang, G. Wang, J. Mater. Chem. A 2019, 7, 6507.
- [18] L. Li, M. Zhang, X. Zhang, Z. Zhang, J. Power Sources 2017, 364, 234.
- [19] Q. Wang, S. Wang, X. Guo, L. Ruan, N. Wei, Y. Ma, J. Li, M. Wang, W. Li, W. Zeng, Adv. Electron. Mater. 2019, 5, 1900537.
- [20] X. Zhang, R. Lv, A. Wang, W. Guo, X. Liu, J. Luo, Angew. Chem. 2018, 130, 15248.
- [21] S. Zhao, H.-B. Zhang, J.-Q. Luo, Q.-W. Wang, B. Xu, S. Hong, Z.-Z. Yu, ACS Nano 2018, 12, 11193.
- [22] M. Han, X. Yin, K. Hantanasirisakul, X. Li, A. Iqbal, C. B. Hatter, B. Anasori, C. M. Koo, T. Torita, Y. Soda, Adv. Opt. Mater. 2019, 7, 1900267.
- [23] P. Sambyal, A. Iqbal, J. Hong, H. Kim, M.-K. Kim, S. M. Hong, M. Han, Y. Gogotsi, C. M. Koo, ACS Appl. Mater. Interfaces 2019, 11, 38046
- [24] X. Wu, B. Han, H.-B. Zhang, X. Xie, T. Tu, Y. Zhang, Y. Dai, R. Yang, Z.-Z. Yu, Chem. Eng. J. 2020, 381, 122622.
- [25] Z. Zeng, C. Wang, G. Siqueira, D. Han, A. Huch, S. Abdolhosseinzadeh, J. Heier, F. Nüesch, C. Zhang, G. Nyström, Adv. Sci. 2020, 7, 2000979.
- [26] R. Bian, G. He, W. Zhi, S. Xiang, T. Wang, D. Cai, J. Mater. Chem. C 2019, 7, 474.





www.advmat.de

- [27] M. Yang, Y. Yuan, Y. Li, X. Sun, S. Wang, L. Liang, Y. Ning, J. Li, W. Yin, Y. Li, ACS Appl. Mater. Interfaces 2020, 12, 33128.
- [28] L. Bi, Z. Yang, L. Chen, Z. Wu, C. Ye, J. Mater. Chem. A 2020, 8, 20030.
- [29] L. Wang, M. Zhang, B. Yang, J. Tan, X. Ding, ACS Nano 2020, 14, 10633.
- [30] Y. Hu, H. Zhuo, Q. Luo, Y. Wu, R. Wen, Z. Chen, L. Liu, L. Zhong, X. Peng, R. Sun, J. Mater. Chem. A 2019, 7, 10273.
- [31] C. Cai, Z. Wei, Y. Huang, Y. Fu, Chem. Eng. J. 2020, 421, 127772.
- [32] P. Lin, J. Xie, Y. He, X. Lu, W. Li, J. Fang, S. Yan, L. Zhang, X. Sheng, Y. Chen, Sol. Energy Mater. Sol. Cells 2020, 206, 110229.
- [33] N.-N. Wang, H. Wang, Y.-Y. Wang, Y.-H. Wei, J.-Y. Si, A. C. Y. Yuen, J.-S. Xie, B. Yu, S.-E. Zhu, H.-D. Lu, ACS Appl. Mater. Interfaces 2019, 11, 40512.
- [34] Q. Zhang, G. Yi, Z. Fu, H. Yu, S. Chen, X. Quan, ACS Nano 2019, 13, 13196.
- [35] W. Yang, J. J. Byun, J. Yang, F. P. Moissinac, Y. Peng, G. Tontini, R. A. Dryfe, S. Barg, Energy Environ. Mater. 2020, 3, 380.
- [36] C. Zhu, T. Liu, F. Qian, W. Chen, S. Chandrasekaran, B. Yao, Y. Song, E. B. Duoss, J. D. Kuntz, C. M. Spadaccini, Nano Today 2017, 15, 107.
- [37] P. Chang, H. Mei, S. Zhou, K. G. Dassios, L. Cheng, J. Mater. Chem. A 2019, 7, 4230.
- [38] X. Li, H. Li, X. Fan, X. Shi, J. Liang, Adv. Energy Mater. 2020, 10, 1903794.
- [39] W. Yang, J. Yang, J. J. Byun, F. P. Moissinac, J. Xu, S. J. Haigh, M. Domingos, M. A. Bissett, R. A. Dryfe, S. Barg, Adv. Mater. 2019, 31, 1902725.
- [40] L. Yu, W. Li, C. Wei, Q. Yang, Y. Shao, J. Sun, Nano-Micro Lett. 2020, 12, 143.
- [41] E. Brown, P. Yan, H. Tekik, A. Elangovan, J. Wang, D. Lin, J. Li, Mater. Des. 2019, 170, 107689.
- [42] P. Yan, E. Brown, Q. Su, J. Li, J. Wang, C. Xu, C. Zhou, D. Lin, Small 2017, 13, 1701756.
- [43] Q. Zhang, F. Zhang, S. P. Medarametla, H. Li, C. Zhou, D. Lin, Small 2016, 12, 1702.
- [44] C. Ma, R. Wang, H. Tetik, S. Gao, M. Wu, Z. Tang, D. Lin, D. Ding, W. Wu, Nano Energy 2019, 66, 104124.
- [45] H. Tetik, K. Zhao, N. Shah, D. Lin, J. Manuf. Processes 2021, 68, 445.
- [46] M. Ghidiu, M. R. Lukatskaya, M.-Q. Zhao, Y. Gogotsi, M. W. Barsoum, Nature 2014, 516, 78.
- [47] H. Tetik, G. Yang, W. Tan, A. Fong, S. Lei, J. N. Weker, D. Lin, Addit. Manuf. 2020, 101513.
- [48] J. Zhang, N. Kong, D. Hegh, K. A. S. Usman, G. Guan, S. Qin, I. Jurewicz, W. Yang, J. M. Razal, ACS Appl. Mater. Interfaces 2020, 12, 24032
- [49] L. Yan, J. Wu, L. Zhang, X. Liu, K. Zhou, B. Su, Mater. Sci. Eng., C 2017, 75, 335.
- [50] R. Dash, Y. Li, A. J. Ragauskas, Carbohydr. Polym. 2012, 88, 789.
- [51] Y. Zhang, K. Zuo, Y.-P. Zeng, Ceram. Int. 2009, 35, 2151.
- [52] L. Hu, C.-A. Wang, Y. Huang, C. Sun, S. Lu, Z. Hu, J. Eur. Ceram. Soc. 2010, 30, 3389.
- [53] Y. Ma, Y. Yue, H. Zhang, F. Cheng, W. Zhao, J. Rao, S. Luo, J. Wang, X. Jiang, Z. Liu, ACS Nano 2018, 12, 3209.

- [54] C. Zhu, T. Y.-J. Han, E. B. Duoss, A. M. Golobic, J. D. Kuntz, C. M. Spadaccini, M. A. Worsley, *Nat. Commun.* **2015**, *6*, 6962.
- [55] L. Qiu, J. Z. Liu, S. L. Chang, Y. Wu, D. Li, Nat. Commun. 2012, 3, 1241.
- [56] D. Wang, Y. Lin, D. Hu, P. Jiang, X. Huang, Composites, Part A 2020, 130, 105754.
- [57] Y. Xia, T. S. Mathis, M.-Q. Zhao, B. Anasori, A. Dang, Z. Zhou, H. Cho, Y. Gogotsi, S. Yang, *Nature* 2018, 557, 409.
- [58] A. Cuna, N. Tancredi, J. Bussi, V. Barranco, T. A. Centeno, A. Quevedo, J. M. Rojo, J. Electrochem. Soc. 2014, 161, A1806.
- [59] Y.-Y. Peng, B. Akuzum, N. Kurra, M.-Q. Zhao, M. Alhabeb, B. Anasori, E. C. Kumbur, H. N. Alshareef, M.-D. Ger, Y. Gogotsi, Energy Environ. Sci. 2016, 9, 2847.
- [60] M. R. Lukatskaya, S. Kota, Z. Lin, M.-Q. Zhao, N. Shpigel, M. D. Levi, J. Halim, P.-L. Taberna, M. W. Barsoum, P. Simon, *Nat. Energy* 2017, 2, 17105.
- [61] Z. Bo, W. Zhu, W. Ma, Z. Wen, X. Shuai, J. Chen, J. Yan, Z. Wang, K. Cen, X. Feng, Adv. Mater. 2013, 25, 5799.
- [62] N. Kurra, B. Ahmed, Y. Gogotsi, H. N. Alshareef, Adv. Energy Mater. 2016, 6, 1601372.
- [63] A. M. Navarro-Suárez, K. Maleski, T. Makaryan, J. Yan, B. Anasori, Y. Gogotsi, Batteries Supercaps 2018, 1, 33.
- [64] C. Zhao, Q. Wang, H. Zhang, S. Passerini, X. Qian, ACS Appl. Mater. Interfaces 2016, 8, 15661.
- [65] Y. Yue, N. Liu, Y. Ma, S. Wang, W. Liu, C. Luo, H. Zhang, F. Cheng, J. Rao, X. Hu, ACS Nano 2018, 12, 4224.
- [66] Z. Zhou, W. Panatdasirisuk, T. S. Mathis, B. Anasori, C. Lu, X. Zhang, Z. Liao, Y. Gogotsi, S. Yang, Nanoscale 2018, 10, 6005.
- [67] E. Quain, T. S. Mathis, N. Kurra, K. Maleski, K. L. Van Aken, M. Alhabeb, H. N. Alshareef, Y. Gogotsi, Adv. Mater. Technol. 2019, 4, 1800256.
- [68] L. Yu, Z. Fan, Y. Shao, Z. Tian, J. Sun, Z. Liu, Adv. Energy Mater. 2019, 9, 1901839.
- [69] H. Li, X. Li, J. Liang, Y. Chen, Adv. Energy Mater. 2019, 9, 1803987.
- [70] J. Zhao, Y. Zhang, Y. Huang, X. Zhao, Y. Shi, J. Qu, C. Yang, J. Xie, J. Wang, L. Li, J. Mater. Chem. A 2019, 7, 972.
- [71] Y. Yoon, K. Lee, S. Kwon, S. Seo, H. Yoo, S. Kim, Y. Shin, Y. Park, D. Kim, J.-Y. Choi, ACS Nano 2014, 8, 4580.
- [72] G. Wang, L. Zhang, J. Zhang, Chem. Soc. Rev. 2012, 41, 797.
- [73] C. J. Zhang, L. McKeon, M. P. Kremer, S.-H. Park, O. Ronan, A. Seral-Ascaso, S. Barwich, C. Ó. Coileáin, N. McEvoy, H. C. Nerl, Nat. Commun. 2019, 10, 1795.
- [74] C. Zhang, M. P. Kremer, A. Seral-Ascaso, S. H. Park, N. McEvoy, B. Anasori, Y. Gogotsi, V. Nicolosi, Adv. Funct. Mater. 2018, 28, 1705506
- [75] S. Abdolhosseinzadeh, R. Schneider, A. Verma, J. Heier, F. Nüesch, C. Zhang, Adv. Mater. 2020, 32, 2000716.
- [76] H. Tetik, D. Lin, International Manufacturing Science and Engineering Conference, American Society of Mechanical Engineers, New York 2020.
- [77] Z. Ling, C. E. Ren, M.-Q. Zhao, J. Yang, J. M. Giammarco, J. Qiu, M. W. Barsoum, Y. Gogotsi, *Proc. Natl. Acad. Sci. USA* 2014, 111, 16676.